

Geophysical Research Letters®



RESEARCH LETTER

10.1029/2022GL098635

Key Points:

- Artificial neural networks skillfully predict sea surface temperatures on decadal timescales in Community Earth System Model, version 2
- The networks identify predictability by assigning lower uncertainty to initial states that lead to lower prediction error
- More predictable initial states coincide with combinations of phases of large scale decadal variability

Supporting Information:

Supporting Information may be found in the online version of this article.

Correspondence to:

E. M. Gordon,
emily.m.gordon95@gmail.com

Citation:

Gordon, E. M., & Barnes, E. A. (2022). Incorporating uncertainty into a regression neural network enables identification of decadal state-dependent predictability in CESM2. *Geophysical Research Letters*, 49, e2022GL098635. <https://doi.org/10.1029/2022GL098635>

Received 10 MAR 2022

Accepted 15 JUL 2022

Author Contributions:

Conceptualization: Emily M. Gordon, Elizabeth A. Barnes

Formal analysis: Emily M. Gordon

Investigation: Emily M. Gordon

Methodology: Emily M. Gordon, Elizabeth A. Barnes

Supervision: Elizabeth A. Barnes

Visualization: Emily M. Gordon

Writing – original draft: Emily M. Gordon

Writing – review & editing: Emily M. Gordon, Elizabeth A. Barnes

© 2022. The Authors.

This is an open access article under the terms of the [Creative Commons Attribution License](https://creativecommons.org/licenses/by/4.0/), which permits use, distribution and reproduction in any medium, provided the original work is properly cited.

Incorporating Uncertainty Into a Regression Neural Network Enables Identification of Decadal State-Dependent Predictability in CESM2

Emily M. Gordon¹  and Elizabeth A. Barnes¹ 

¹Department of Atmospheric Science, Colorado State University, Fort Collins, CO, USA

Abstract Predictable internal climate variability on decadal timescales (2–10 years) is associated with large-scale oceanic processes, however these predictable signals may be masked by the noisy climate system. One approach to overcoming this problem is investigating state-dependent predictability—how differences in prediction skill depend on the initial state of the system. We present a machine learning approach to identify state-dependent predictability on decadal timescales in the Community Earth System Model version 2 pre-industrial control simulation by incorporating uncertainty estimates into a regression neural network. We leverage the network's prediction of uncertainty to examine state dependent predictability in sea surface temperatures by focusing on predictions with the lowest uncertainty outputs. In particular, we study two regions of the global ocean—the North Atlantic and North Pacific—and find that skillful initial states identified by the neural network correspond to particular phases of Atlantic multi-decadal variability and the interdecadal Pacific oscillation.

Plain Language Summary As the climate warms with anthropogenic climate change, it is increasingly important to predict long term climate variability in order to prepare for possible extremes. However, the Earth's climate is chaotic and deciphering predictable long-term signals from this noisy system has proven challenging. Here we leverage times where predictable signals rise above the noise and the long-term forecasts have less error. We present a machine learning approach to identify these times when the climate is more predictable and show that these are related to particular patterns of heat in the Atlantic and Pacific Oceans.

1. Introduction

Predicting the evolution of the climate on decadal timescales (2–10 years) has far reaching implications for both climate science and society. On these timescales, changes in climate patterns are associated with the forced response to anthropogenic emissions and internal variability in the ocean (Meehl et al., 2021). For example, the forced response from climate change can manifest as the steady increase of global mean temperature which provides some predictability of future temperatures. Decadal predictability of oceanic temperature variability arises from the ocean's ability to store, release and transport heat on decadal timescales. Major modes of variability in the Pacific and Atlantic Oceans are therefore linked to decadal predictability as they indicate the spatial distribution of heat in these basins. Furthermore, this internal variability in the ocean can act to either mask or amplify the forced response from climate change (Trenberth & Fasullo, 2013). The Pacific Ocean exhibits long-term variability via the interdecadal Pacific oscillation (IPO Meehl et al., 2013; Power et al., 1999) and its related mode Pacific decadal variability (PDV, Mantua et al., 1997; Zhang et al., 1997). Atlantic multi-decadal variability (AMV, Enfield et al., 2001; Xie & Tanimoto, 1998) is considered the dominant form of long-term variability in the Atlantic ocean, however whether variability arises due to internal Earth system processes or external forcing is still under debate (Booth et al., 2012; Clement et al., 2015; Mann et al., 2021). Because these patterns of variability are associated with decadal predictability, decadal prediction is traditionally focused on either investigating and predicting the processes themselves, (e.g., Meehl et al., 2016; Gordon et al., 2021; Zhang et al., 2019), or exploring the predictability that arises from the atmospheric teleconnections driven by these patterns (e.g., Zhang & Delworth, 2006; Simpson et al., 2018, 2019).

As hinted at above, it is difficult to decipher the drivers of predictability in observations and historical simulations as it is influenced by the non-linear interactions between internal variability and external forcing. Studies have diagnosed predictability in pre-industrial control runs (Branstator et al., 2012), while others have deciphered

predictability from internal variability in model hindcast ensembles with accompanying un-initialized ensembles (Borchert et al., 2021; Yeager et al., 2018). Another avenue of research has been to quantify (using various metrics) how much predictability is present in different regions of the ocean, and what the relative contributions of internal and external drivers may be (Boer, 2011; Branstator & Teng, 2010). However, predictability in the climate system can vary drastically depending on region, timescale, and initial state (Christensen et al., 2020; Mariotti et al., 2020; Meehl et al., 2021) thus studies have encouraged a shift of focus toward the concept of state-dependent predictability (Mariotti et al., 2020; Merryfield et al., 2020; Msadek et al., 2010; Pohlmann et al., 2004). This paradigm intrinsically acknowledges that some initial states lead to more predictable behavior than others. The aim is therefore to identify these more predictable initial states, as they provide the opportunity to make more skillful forecasts. State-dependent predictability has been investigated on short (subseasonal to seasonal) timescales as the identification of “forecasts of opportunity” (Albers & Newman, 2019; Mayer & Barnes, 2021). An example of an oceanic region with decadal state-dependent predictability is the North Atlantic Subpolar Gyre. It has been found that anomalously strong ocean heat transport in the North Atlantic ocean is associated with skillful predictions of sea surface temperature (SST) in the North Atlantic Subpolar Gyre for lead times up to 8 years (Borchert et al., 2018; Brune et al., 2018). So enhanced heat transport in the North Atlantic could be considered a more predictable initial state for predicting North Atlantic SSTs.

With this increased focus on state-dependent predictability, it is necessary to explore methods that can identify state-dependent predictability. Machine learning is one such method that shows promise for identifying more predictable initial states. In fact, on subseasonal timescales, classification artificial neural networks (ANNs) have been shown to objectively identify states of the Madden-Julian oscillation that lead to enhanced predictability of circulation in the North Atlantic (Mayer & Barnes, 2021) by leveraging the network's confidence in a prediction to identify state-dependent predictability. Furthermore, on decadal timescales it has been demonstrated that ANNs can skillfully predict decadal processes (Gordon et al., 2021; Labe & Barnes, 2022) and identify states of enhanced predictability of surface temperature over land (Toms et al., 2021).

This study introduces the identification of state-dependent predictability on decadal timescales using a regression-based neural network to predict sea surface temperatures (SSTs) across the globe within the Community Earth System Model, version 2 (CESM2, Danabasoglu et al., 2020) pre-industrial control simulation. We demonstrate a powerful technique for incorporating uncertainty into the prediction of regression neural networks which has previously only been used a handful of times in climate science (Barnes & Barnes, 2021; Foster et al., 2021; Guillaumin & Zanna, 2021). We further leverage this uncertainty output to identify which initial states are associated with the lower uncertainty predictions. Lower uncertainty predictions imply more predictable inputs, hence this technique identifies state-dependent predictability. Furthermore, we link predictable initial states to major forms of variability so we are able to identify certain combinations of IPO and AMV phases that correspond to skillful decadal predictions of SSTs in CESM2.

2. Data and Methods

2.1. Data

We use sea surface temperature (SST) and ocean heat content (OHC) output from the CESM2 pre-industrial control run for the Coupled Model Intercomparison Project phase 6 (CMIP6; Eyring et al., 2016). OHC is interpolated to a $4^\circ \times 4^\circ$ grid. We train ANNs at each SST grid point so SST is interpolated to a $5^\circ \times 5^\circ$ grid which captures the regional variation in predictability while not being too computationally demanding. We use monthly output of the 2000 year run with the first 100 years removed to allow the ocean circulation to spin-up. Both OHC and SST are then de-seasonalized by removing the mean annual cycle from each grid point. Furthermore, to account for model drift, after deseasonalizing we calculate the third degree polynomial trend via least squares and subtract this from each grid point. This means that each variable's statistics are approximately stationary for the remaining 1900 years of data. OHC is smoothed using a 60 month backward running mean to smooth high frequency variability. We divide the pre-processed data into training, validation and testing. The first 70% (~1300 years) is used for training, the next 15% (~300 years) for validation and the last 15% (~300 years) for testing. We calculate the mean and standard deviation for every point on both the OHC and SST grids in the training set. We then use these values to standardize all of the training, validation and testing data.

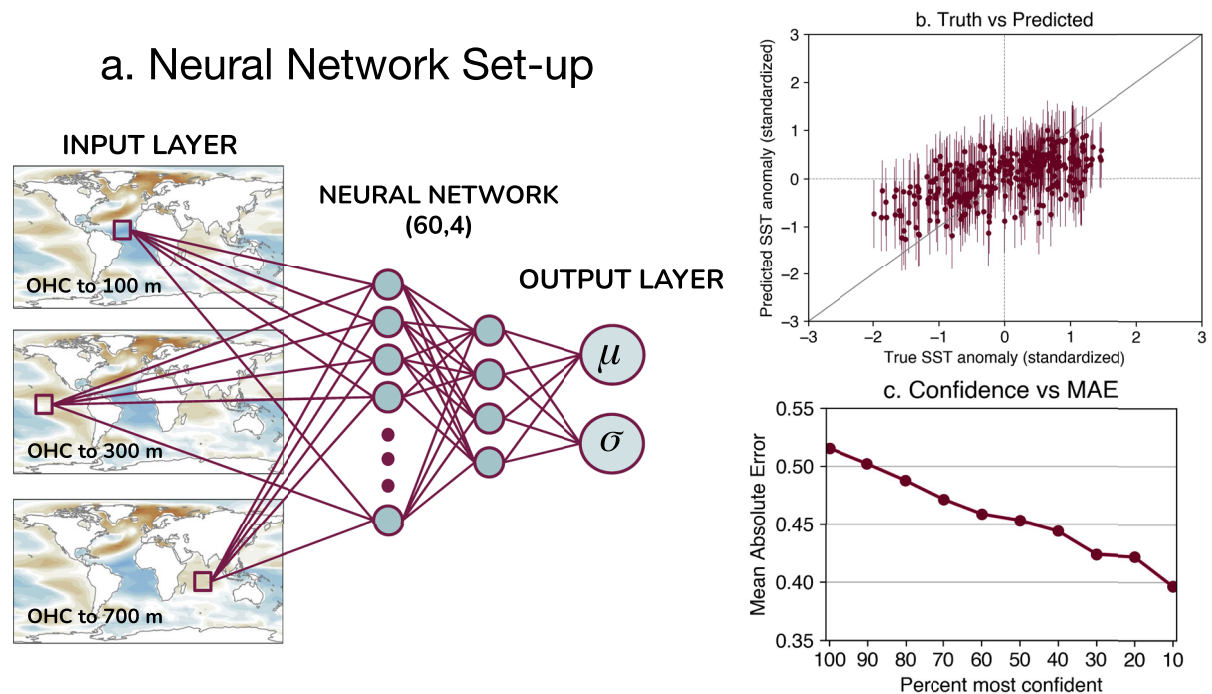


Figure 1. (a) Schematic of the artificial neural network architecture. (b) Scatter plot of predicted sea surface temperature (SST) anomaly (y axis) versus true SST anomaly (x axis). Dots represent predicted μ values, while vertical lines represent the 1σ range. (c) Prediction mean absolute error as a function of prediction confidence (see text). Both (b) and (c) utilize the same network trained to predict SST in the North Atlantic Ocean (52.5°N, 325°E).

2.2. Artificial Neural Network

Artificial neural networks (ANNs) are used to predict the average SST anomaly at a lead time of 1–5 years and 3–7 years, that is, the ANN predicts the average 60 month SST anomaly in the next 12–72 months, or 36–96 months respectively. In this experiment the ANN is trained to predict the SST evolution in the CESM2 pre-industrial control, so for example, one input sample is OHC information from a specific time step in the control run, and the output prediction is the average SST anomaly over the next 12–72 months in the control run. A schematic of our neural network architecture is provided in Figure 1a and a brief overview of ANNs for geoscience applications can be found in for example, Toms et al. (2020). The predictors are three OHC grids, where each grid is OHC integrated to a different depth (100, 300 and 700 m). We chose varying depths of OHC because each contains information corresponding to different forms of climate variability. For example, the upper levels of the ocean integrate atmospheric forcing, and hence capture atmospheric variability as well as surface ocean dynamics (Frankignoul & Hasselmann, 1977). The variability in lower levels of the ocean is guided by a combination of slow moving ocean circulation and the incorporation of mixed layer processes via the annual cycle in the thermocline (Alexander & Deser, 1995). By inputting three OHC depths into the neural network, it can theoretically combine different oceanic and atmospheric processes to make its predictions. The three ocean grids are vectorized with points over land removed resulting in a total 7947 input pixels. This input is connected to a hidden layer of 60 nodes which is then connected to another hidden layer of 4 nodes (see Figure 1). In this network, all layers are densely connected meaning all nodes in the previous layer are connected to all the nodes in the next layer. Furthermore, all nodes in the hidden layers use the rectified linear unit (ReLU) activation function. Finally this second layer is connected to the output layer of two nodes which serve as the parameters of the predicted conditional distribution (see details in the next paragraph). Here the distribution is a normal distribution as we found allowing skewness did not significantly improve the network's performance (not shown).

We use the $-\log(p)$ loss function described by for example, Barnes et al. (2021) which we will summarize briefly. For each input, the network outputs two values, μ and σ . To calculate loss, μ and σ are used to construct a conditional distribution, d and the negative log likelihood function is calculated at the true value (y_{true}), that is, $\text{loss} = -\log(p(y_{\text{true}}|d))$. This means that the neural network can decrease loss (decrease $-\log(p(y_{\text{true}}|d))$) in different ways: either with a low σ value and μ that is close to y_{true} , or predict a larger σ value with μ that is further from

y_{true} , or both. The neural network is therefore not penalized for high error predictions as long as it also guesses a correspondingly high σ value, that is, if it recognizes an input is less predictable by assigning a high σ value. The predictions of such an ANN are illustrated in Figure 1b, where we show an example scatter plot of prediction versus truth from an ANN trained to predict SST anomaly in the North Atlantic Subpolar Gyre. Note that we can plot both the predicted anomaly value (μ , colored dots) and an uncertainty range, with the error bars indicating the $\pm 1\sigma$ range predicted by the ANN. The ANN is trained using the training set, with the validation set evaluated at the end of each epoch. The results presented in this study are from the testing set. During training, we use a learning rate of 1×10^{-4} with stochastic gradient descent for up to 1,000 epochs with early stopping when validation loss did not decrease for 100 epochs. To implement regularization, we include a dropout layer between the input layer and first hidden layer in training. We found that a high rate of dropout (80% dropout rate in this experiment) forced the ANN to learn information more slowly and greatly reduced over-fitting on the validation set.

2.3. AMV and IPO Indices

We compute the AMV and IPO indices within CESM2 using the deseasoned and detrended SST data. For the AMV index, we calculate the monthly mean SST anomaly over the North Atlantic ocean (0°N to 80°N , 280°E to 360°E) and then standardize by removing the mean and dividing by the standard deviation. Note we do not de-trend by the global mean SST as recommended by Trenberth and Shea (2006) because the control run lacks a forced long term warming trend and model drift was removed during pre-processing. We calculate the IPO index following the tripole index proposed by Henley et al. (2015). We include plots of the spatial AMV and IPO patterns in CESM2 and the method for calculating IPO index in Supporting Information S1.

3. Results

3.1. Evaluating Performance

In this study, 10 networks (identical architecture, only varying the initial network random seed) are trained at each SST grid point in the ocean and we show the results of the best neural network at each grid point. To designate the “best” network, we select the ANN with the lowest mean absolute error (MAE, difference between predicted μ and true y) on the 10% of samples with the lowest σ predictions in the validation set. This designation leverages a fundamental characteristic of a network that has learned predictability in the data: prediction error should decrease as predicted σ decreases. We demonstrate this idea in Figure 1c where we show a network trained to predict SST in 1–5 years in the North Atlantic (52.5°N , 325°E). Along the x -axis, we threshold by increasing confidence (we define more confident predictions as those with lower uncertainty) with the y -axis showing corresponding MAE for those predictions. For all samples, the MAE is ~ 0.52 however for the 40% most confident predictions the MAE has dropped to 0.46. For the 10% most confident predictions, the MAE has dropped further to ~ 0.39 implying the network has learned samples that lead to more predictable SST anomaly. We hence refer to lower σ predictions as more confident predictions, or more predictable inputs. For some grid points, all networks fail to learn anything, meaning they always predict an SST anomaly of zero (or very close to zero). These networks are removed before analysis, resulting in 30% of networks (525/1709) removed for lead years 1–5, and 39% (675/1709) for lead years 3–7.

3.2. Predicting SST

We ensure that the ANNs are learning to skillfully predict SSTs on decadal timescales in CESM2 by examining prediction error in the testing data at each grid point. Figure 2a is the MAE for ANN predictions for the testing set for lead years 1–5, with black indicating grid points where all 10 networks failed to learn anything. These regions are largely in the Southern Hemisphere subtropics, and the lowest MAEs are found in the North Atlantic Ocean and the Southern Ocean around South America. This spatial distribution of prediction skill (including regions where the networks failed) broadly agrees with that found to be attributable to internal variability in the decadal hindcast studies using the CESM1 decadal prediction large ensemble (Christensen et al., 2020; Yeager et al., 2018). These studies use a different model version (CESM1 vs. CESM2), and the simulations include the effects of external forcing since 1850. However, the widespread agreement of spatially varying predictability suggests the results in Figure 2 are not a result of experiment design or network architecture but are rather due to differences in predictability between regions.

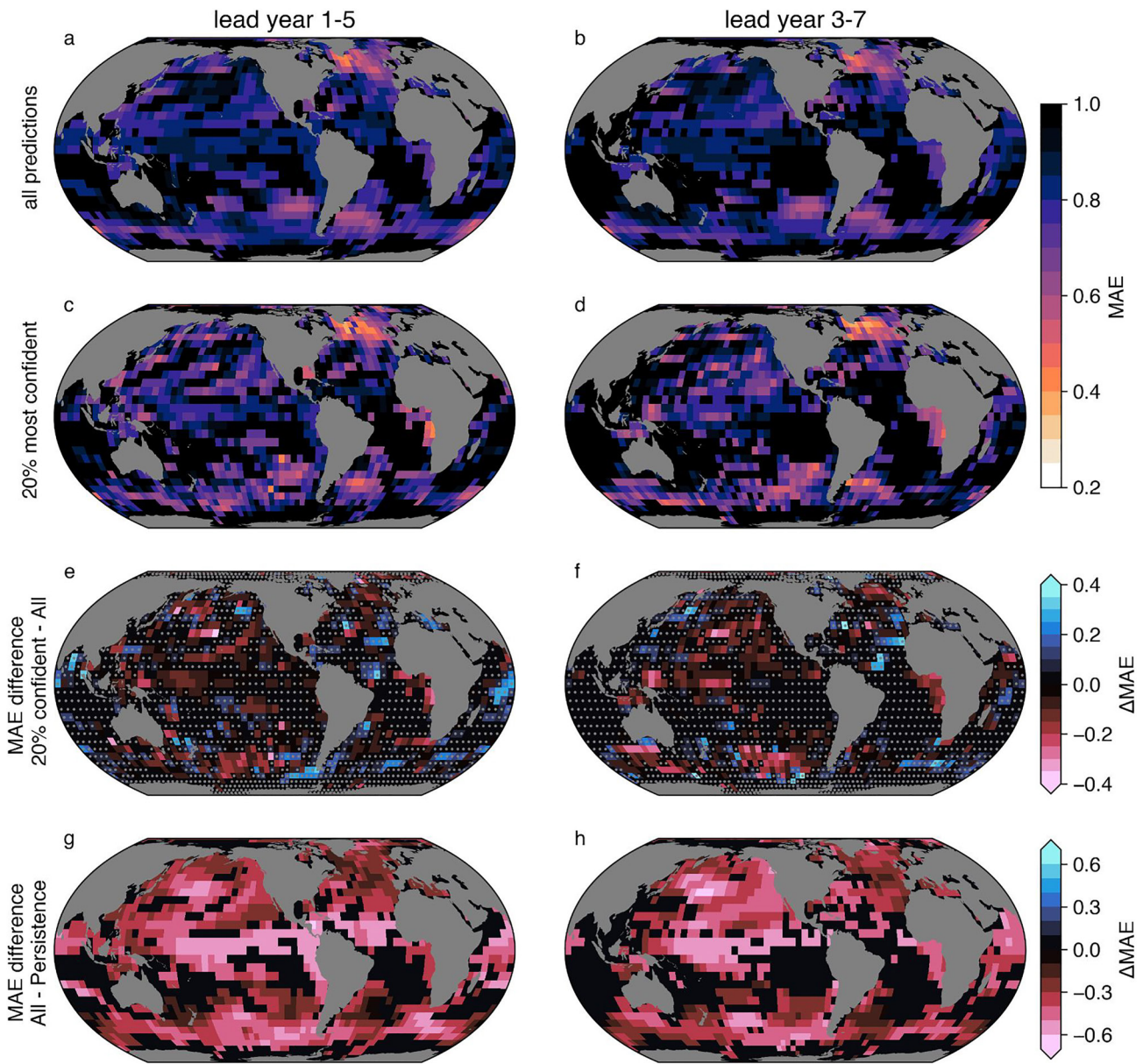


Figure 2. Evaluation of artificial neural networks (ANN) prediction error. The left column is the prediction error for lead years 1–5, and the right column is for lead years 3–7. Panels (a and b) are mean absolute error (MAE) for all predictions in the testing set (i.e., all samples, $N = 3400$). Panels (c and d) show MAE for only the 20% most confident predictions in the testing set as identified using the ANNs's uncertainty ($N = 680$). Panels (e and f) are the differences between the 20% most confident predictions and all predictions (e.g., panel e = panel c – a). Stippling indicates areas where the skill improvement is not statistically significant to $\alpha = 0.05$. Panels (f and g) are the difference between MAE_{ANN} and $MAE_{persistence}$ ($MAE_{ANN} - MAE_{persistence}$) in the testing set.

The prediction skill for lead years 3–7 is shown in Figure 2b and highlights similar regions as being more predictable as in lead years 1–5. Furthermore, there does not seem to be a substantial loss in skill between these two lead times. This, coupled with the spatial distribution of prediction skill, suggests that the ANNs are learning physical relationships to make their predictions.

To contextualize the predictions of the ANNs, we benchmark them against a simple persistence model. The persistence model predicts that the SST anomaly will be unchanged so that the SST anomaly at the time of input remains the same at the time of prediction. We calculate the MAE for the persistence model and subtract it from the MAE of the ANNs ($\Delta MAE = MAE_{ANN} - MAE_{persistence}$), and plot the results in Figures 2g and 2h. In regions where ΔMAE is negative, the ANN outperforms persistence (i.e., has lower error). These regions are

illustrated in warm colors in Figures 2g and 2h and illustrates that the ANNs trained in this study out-perform persistence in all locations and at both lead times. Using a null hypothesis of $\Delta\text{MAE} = 0$, the MAE differences in these regions are significantly different from zero (i.e., the null hypothesis can be rejected) using a one-sided Wilcoxon signed-rank test with $\alpha = 0.05$. The greatest improvement in skill above persistence occurs in the cold tongue region of the Equatorial Pacific. This is unsurprising as this region exhibits large interannual variability due to the El Niño Southern Oscillation, and hence persistence performs poorly in this region. Also notable, the improvements over persistence do not necessarily align with grid points where the networks achieve lowest MAE. This is a fingerprint of regional decadal variability, that regions with longer memory (e.g., the mid-latitude North Atlantic) are better modeled by persistence, but in these cases our networks still out-perform persistence.

3.3. Identifying State-Dependent Predictability

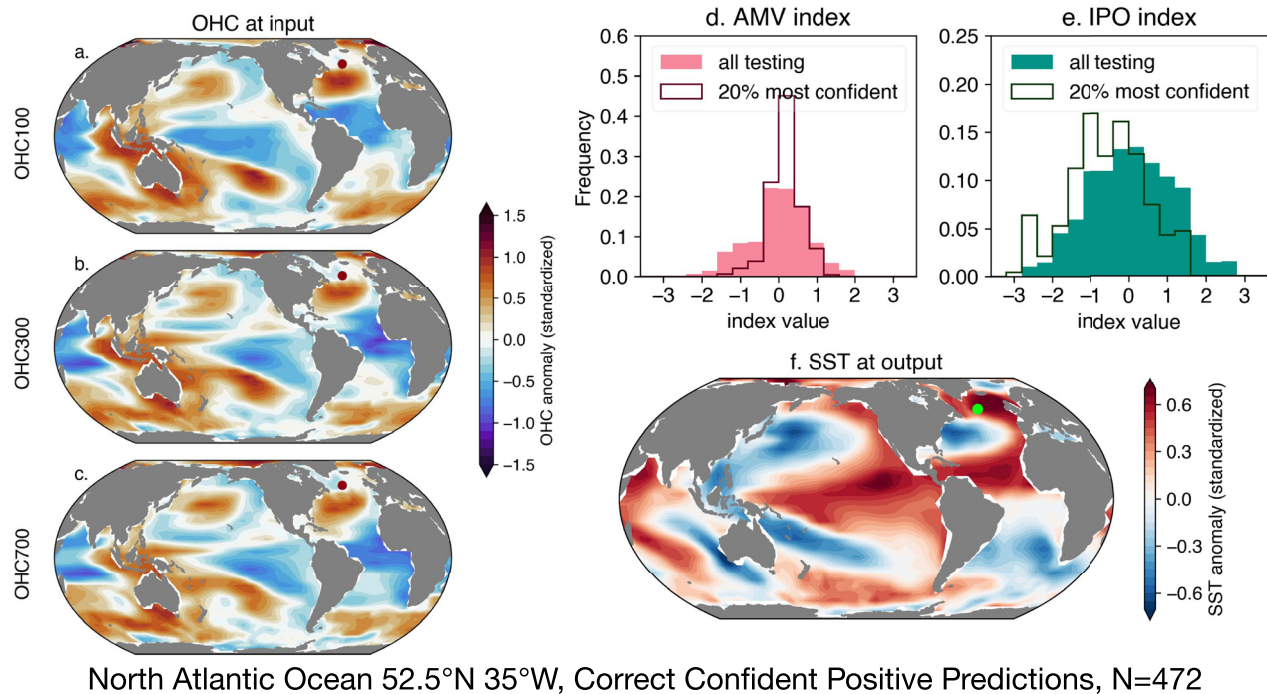
The predictive power of ANNs for decadal prediction is now demonstrated by using them to identify state-dependent predictability. In Figures 2c and 2d we plot the MAE for only the 20% most confident predictions (20% lowest predicted σ) by the ANN for each SST grid point. That is, ANN objectively identifies more predictable initial states, and we do not directly use knowledge of the ground truth to identify these predictions. To aid in visualization, we also plot the difference in MAE between the 20% confident predictions and all predictions in Figure 2e. When comparing the most confident predictions with all predictions at lead years 1–5 (Figure 2e), MAE is largely reduced for more confident predictions in the mid-latitudes, implying that more confident predictions are associated with smaller prediction errors in these locations. Similarly for lead year 3–7 (Figure 2f), we see that sorting for the most confident predictions leads to reduced error in most locations. For those regions where error increases, this is likely due to the network learning predictability in the testing and validation data that does not generalize to the testing data which either suggests over-fitting or unaccounted-for model drift. Interestingly, at both lead times, some regions that show very little skill across all predictions exhibit large increases in skill when considering only the most confident predictions (e.g., central Pacific and the Gulf of Guinea), demonstrating that a region may be considered not predictable when in fact it is just not *always* predictable.

3.4. Investigating Skillful Decadal Predictions

By using ANN predictions to identify state-dependent predictability, we can also investigate oceanic patterns that lead to predictability. Here we examine the predictions of two ANNs trained to predict SSTs in the North Atlantic and North Pacific oceans to investigate processes that are contributing to enhanced prediction skill in these regions. In the following analysis we single out two particular grid points to investigate SST predictability but the results are largely unchanged for the directly adjacent grid cells. Here, we show results for the testing data but these results are consistent throughout the control run (see Supporting Information S1).

Figure 3 shows the 20% most confident predictions of positive SST anomaly for a point in the North Atlantic Sub-Polar Gyre from the testing set (52.5°N, 325°E). We single out positive predictions because the ANN's confident predictions are preferentially positive (583 positive predictions out of 680 confident testing samples, where 680 is 20% of the testing set), implying that the ANN detects that particular positive predictions lead to lower uncertainty. As predictions are preferentially positive, this is evidence that the ANN is detecting state-dependent predictability in the North Atlantic.

We plot the correct and confident positive predictions to ensure we are analyzing the correct signals that contribute to predictability. This leaves 472 samples. Figures 3a–3c show the composite of OHC input maps for correct and confident positive predictions to investigate the initial states that lead to predictability. At all three OHC levels there is a positive OHC anomaly in the subtropical to mid-latitude Atlantic Ocean. We verify that this signal was likely utilized by the ANN in its predictions by using an ANN explainability technique to investigate the input regions that are important to the network's prediction (see Text S1 and Figure S2 in Supporting Information S1). This shows the positive OHC anomaly in the North Atlantic at all three OHC levels was highlighted as contributing to the ANN's decisions. As the positive heat anomaly is slightly south of the predicted grid point, this could indicate northward heat transport to achieve a positive prediction. The composite SST anomaly in Figure 3f shows the positive anomaly is around the predicted grid point in the North Atlantic which implies that this anomaly has moved northward from the initial state (i.e., northward from the positive OHC anomaly in the subtropical North Atlantic in Figure 3a). From this evidence, we posit that the skillful SST prediction is preceded



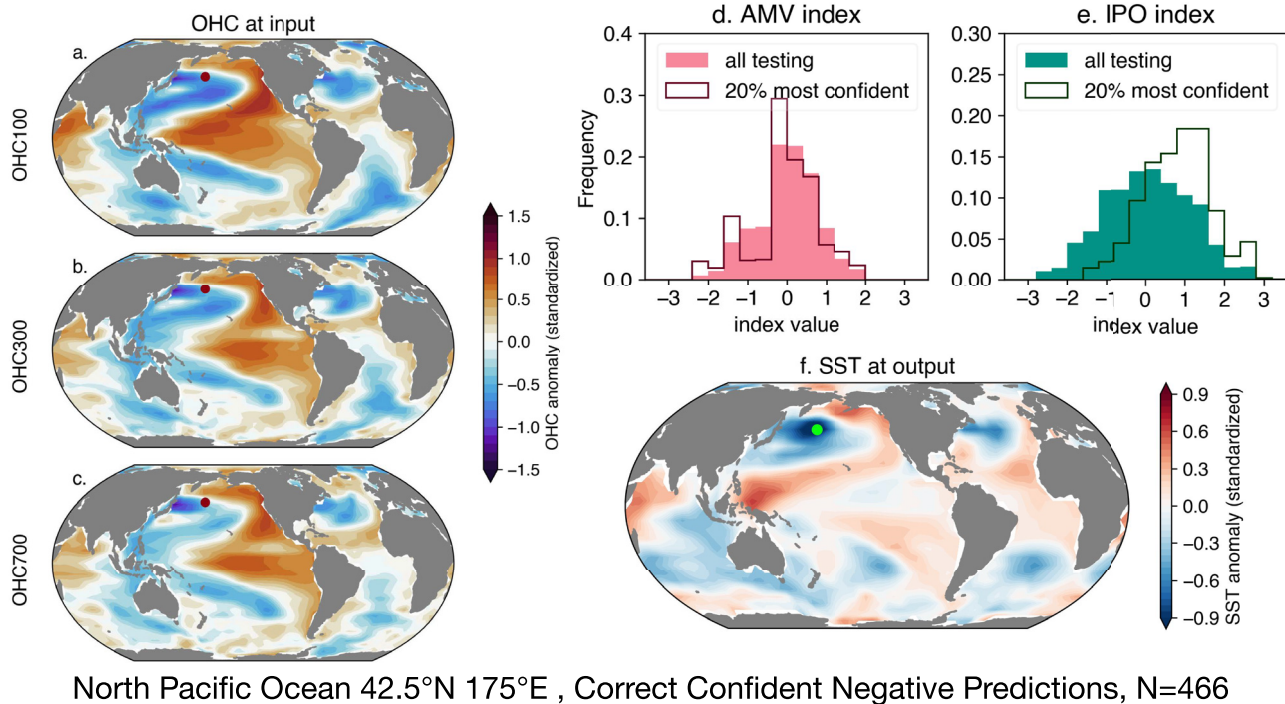
North Atlantic Ocean 52.5°N 35°W, Correct Confident Positive Predictions, N=472

Figure 3. State-dependent predictability identified in the North Atlantic for predicting average sea surface temperature (SST) anomaly at lead time 1–5 years. Panels (a–c): Composite of ocean heat content inputs for confident predictions of positive SST anomaly in a point in the North Atlantic (red dot). Panel (d): histogram of Atlantic multi-decadal variability index for testing data (pink shading) and most confident predictions (pink outline). Panel (e): as panel (d) but for interdecadal Pacific oscillation index. Panel (f): Composite of SST map for confident predictions of SST in the North Atlantic (green dot).

by a positive heat anomaly in North Atlantic ocean, which is transported into the gyre region. This is consistent with Borchert et al. (2018) who identified periods of enhanced heat transport in the mid-latitude as a state of increased predictability of SSTs in the North Atlantic subpolar gyre for up to 8 years.

As an analogue for oceanic variability, we also consider the phases of the AMV and IPO during periods of increased network confidence. In Figure 3d we present the distribution of the AMV index during the entire testing period (pink shading, mean = 0.00) with the solid line showing the distribution for only 20% confident predictions which has a mean of 0.16. From this, it appears that confident predictions are most likely to occur during positive AMV. When randomly drawing 20% of the samples from the AMV distribution in testing, the likelihood of a mean of 0.16 occurring is less than 1%. This implies that more skillful SST predictions in the North Atlantic Sub-Polar Gyre coincide with northward heat transport from the subtropics (from Figures 3a–3c and 3f) coupled with the positive phase of AMV (from Figure 3d). This is consistent with previous results by for example, Christensen et al. (2020); Borchert et al. (2018). In Figure 3e, we show the distribution of IPO phase for the testing data (green shading, mean = 0.05) and 20% most confident predictions outlined with the solid line, with a mean of −0.58. The likelihood drawing a mean of −0.58 from the IPO testing distribution is less than 1% which suggests that the negative phase of the IPO contributes to the predictability of North Atlantic SSTs. This is also apparent in Figures 3a–3c which all show the negative IPO pattern in the Pacific Ocean. This may indicate some inter-basin teleconnection that contributes to the predictability of North Atlantic SSTs.

We now perform a similar analysis for an ANN trained to predict SST in 1–5 years at a point in the North Pacific (42.5°N, 175°E). In Figure 4 we show the results for the 20% most confident negative predictions. For this region, 632 out of the 680 most confident samples were predictions of negative anomaly, implying the ANN designated negative predictions as more confident. Again we plot only the correct predictions, resulting in 466 samples in these composites. Figures 4a–4c shows the composite OHC inputs for confident negative predictions, and the major signal appears to be a positive IPO/PDV pattern in all panels. It is likely the ANN utilized this pattern to make these confident negative predictions from the ANN explainability heat-maps (see Text S1 and Figure S3 in Supporting Information S1). This is supported by the histogram of the IPO index in Figure 4e which shows the distribution of IPO phase in the confident samples is shifted such that confident samples significantly coincide



North Pacific Ocean 42.5°N 175°E , Correct Confident Negative Predictions, N=466

Figure 4. As Figure 3 but for the North Pacific.

with the positive phase of the IPO. There is no such strong signal in the AMV index (Figure 4d). Lastly, the confident predictions appear to relate to persistence in the positive IPO phase because the composite map of SST at output (Figure 4f) shows an IPO pattern in the Pacific Ocean. The largest SST anomalies are in the north Pacific mid-latitudes, in the traditional PDV region. From this, we posit that skillful predictions of SST in the North Pacific are associated with persistence in the positive phase of IPO (i.e., negative SST anomaly at the predicted grid point). Here, the ANN preferentially identifies negative SST predictions as skillful, perhaps implying that persistence in the positive phase of IPO is more predictable than persistence of the negative phase. We posit that this difference in predictability is due to the underlying non-linear mechanisms governing IPO dynamics and particularly the asymmetry in the dynamics governing ENSO events (Choi et al., 2013; Okumura & Deser, 2010). Further investigation of this is an avenue for future work.

4. Discussion and Conclusion

We show that artificial neural networks (ANNs) skillfully predict SST evolution on decadal timescales and that they can objectively identify decadal state-dependent predictability associated with low-frequency internal variability in the North Pacific and North Atlantic Oceans. Specifically, we use a regression neural network where the predictions take the form of a conditional normal distribution which we leverage to isolate predictions that are more likely to have lower error. This approach allows us to investigate possible contributing mechanisms to decadal SST predictability, particularly Atlantic multi-decadal variability and the interdecadal Pacific oscillation (AMV and IPO, Figures 3 and 4). We chose to model the conditional distributions as normal distributions as alternatives did not significantly improve skill. We suggest that future studies investigating state-dependent predictability for other timescales and variables may benefit from the addition of skewness to the predicted conditional distributions (Barnes et al., 2021), as well as further exploring alternative network architectures to tease out additional skill.

We investigate state-dependent predictability in two regions, the North Atlantic Subpolar Gyre, and the North Pacific Ocean. Predictability is assessed by investigating the processes that correspond to the lowest uncertainty predictions by the ANNs for these two regions. This study utilizes the CESM2 long control representation of the climate system and the results in the North Atlantic appear to agree with hindcast studies of Brune et al. (2018);

Borchert et al. (2018); Yeager et al. (2018) which use different models to that used here (MPI-ESM; Giorgetta et al. (2013) and CESM1; Hurrell et al. (2013)). These previous studies also incorporate observations or reanalysis to evaluate the prediction skill of the decadal hindcasts. Moreover, in a study of initialized decadal hindcasts in the CMIP6 archive, Borchert et al. (2021) attribute predictable SSTs in the North Atlantic subpolar gyre to the effects of external forcing in the historical era, particularly volcanic forcing. Since our findings are consistent with the state-dependent predictability investigated in these studies, this suggests that the ANN predictions and mechanisms investigated here are likely relevant to realistic climate variability and implies a role for internal variability in North Atlantic predictability. Further investigation is left for future work.

Here we present a data-driven approach to diagnosing state-dependent predictability in an unforced model simulation. In addition to the role of North Atlantic heat transport, we find evidence for a state-dependent inter-basin teleconnection, that is, the negative phase of the IPO influencing predictability of North Atlantic SSTs (Figure 3). The drivers of predictability and variability in the North Atlantic ocean are still debated, especially the relative roles of internal variability and external forcing (Clement et al., 2015; Fang et al., 2021; Fenske & Clement, 2022; Mann et al., 2021; Wu et al., 2011; Zhang et al., 2019). We hence suggest that future work on decadal prediction should investigate the roles of internal variability and external forcing through the lens of state-dependent predictability.

This study emphasizes the importance of examining state-dependent predictability for decadal predictions. We stress that the a priori identification of more predictable initial states greatly increases prediction skill and can hence aid in estimating the evolution of the internal long-term variability of the climate system.

Data Availability Statement

We use CESM2 output from the pre-industrial control experiment which is freely available from Earth System Grid <https://esgf-node.llnl.gov/projects/cmip6> (Danabasoglu, 2019). Analysis was carried out in Python 3.7 and 3.9, ANNs were developed using TensorFlow (Abadi et al., 2016), while XAI heatmaps were created with iNNvestigate (Alber et al., 2019). Many color maps in this work are the from CMasher package (van der Velden, 2020) and regridding was achieved using Climate Data Operators (CDO; Schulzweida, 2019). Code used to preprocess, generate the ANNs, and produce the figures in this work can be found at Gordon (2022).

References

- Abadi, M., Barham, P., Chen, J., Chen, Z., Davis, A., Dean, J., et al. (2016). Tensorflow: A system for large-scale machine learning. In *12th USENIX symposium on operating systems design and implementation (OSDI 16)* (pp. 265–283). USENIX Association. Retrieved from <https://www.usenix.org/conference/osdi16/technical-sessions/presentation/abadi>
- Alber, M., Lapuschkin, S., Seegerer, P., Hägele, M., Schütt, K. T., Montavon, G., et al. (2019). Innvestigate neural networks. *Journal of Machine Learning Research*, 20(93), 1–8. Retrieved from <http://jmlr.org/papers/v20/18-540.html>
- Albers, J. R., & Newman, M. (2019). A Priori identification of skillful extratropical subseasonal forecasts. *Geophysical Research Letters*, 46(21), 12527–12536. <https://doi.org/10.1029/2019gl085270>
- Alexander, M. A., & Deser, C. (1995). A mechanism for the recurrence of wintertime midlatitude SST anomalies. *Journal of Physical Oceanography*, 25(1), 122–137. [https://doi.org/10.1175/1520-0485\(1995\)025<0122:AMFTRO>2.0.CO;2](https://doi.org/10.1175/1520-0485(1995)025<0122:AMFTRO>2.0.CO;2)
- Barnes, E. A., & Barnes, R. J. (2021). Controlled abstention neural networks for identifying skillful predictions for regression problems. *Journal of Advances in Modeling Earth Systems*, 13(12). <https://doi.org/10.1029/2021ms002575>
- Barnes, E. A., Barnes, R. J., & Gordillo, N. (2021). Adding uncertainty to neural network regression tasks in the geosciences. Retrieved from <http://arxiv.org/abs/2109.07250>
- Boer, G. J. (2011). Decadal potential predictability of twenty-first century climate. *Climate Dynamics*, 36(5), 1119–1133. <https://doi.org/10.1007/s00382-010-0747-9>
- Booth, B. B., Dunstone, N. J., Halloran, P. R., Andrews, T., & Bellouin, N. (2012). Aerosols implicated as a prime driver of twentieth-century North Atlantic climate variability. *Nature*, 484(7393), 228–232. <https://doi.org/10.1038/nature10946>
- Borchert, L. F., Menary, M. B., Swingedouw, D., Sgubin, G., Hermanson, L., & Mignot, J. (2021). Improved decadal predictions of North Atlantic subpolar gyre SST in CMIP6. *Geophysical Research Letters*, 48(3). <https://doi.org/10.1029/2020gl091307>
- Borchert, L. F., Müller, W. A., & Baehr, J. (2018). Atlantic ocean heat transport influences interannual-to-decadal surface temperature predictability in the north Atlantic region. *Journal of Climate*, 31(17), 6763–6782. <https://doi.org/10.1175/JCLI-D-17-0734.1>
- Branstator, G., & Teng, H. (2010). Two limits of initial-value decadal predictability in a CGCM. *Journal of Climate*, 23(23), 6292–6311. <https://doi.org/10.1175/2010JCLI3678.1>
- Branstator, G., Teng, H., Mehl, G. A., Kimoto, M., Knight, J. R., Latif, M., & Rosati, A. (2012). Systematic estimates of initial-value decadal predictability for six AOGCMs. *Journal of Climate*, 25(6), 1827–1846. <https://doi.org/10.1175/JCLI-D-11-00227.1>
- Brune, S., Düsterhus, A., Pohlmann, H., Müller, W. A., & Baehr, J. (2018). Time dependency of the prediction skill for the North Atlantic subpolar gyre in initialized decadal hindcasts. *Climate Dynamics*, 51(5), 1947–1970. <https://doi.org/10.1007/s00382-017-3991-4>
- Choi, K.-Y., Vecchi, G. A., & Wittenberg, A. T. (2013). ENSO transition, duration, and amplitude asymmetries: Role of the nonlinear wind stress coupling in a conceptual model. *Journal of Climate*, 26(23), 9462–9476. <https://doi.org/10.1175/JCLI-D-13-00045.1>

Acknowledgments

E. M. Gordon is partially funded by Fulbright New Zealand. E. M. Gordon and E. A. Barnes are supported, in part, by NSF CAREER AGS-1749261 under the Climate and Large-scale Dynamics program. We thank John Fasullo at the National Center for Atmospheric Research (NCAR) for diagnosing the OHC from CESM2. We would like to acknowledge high-performance computing support from Cheyenne (<https://doi.org/10.5065/D6RX99HX>) provided by NCAR's Computational and Information Systems Laboratory, sponsored by the National Science Foundation.

- Christensen, H. M., Berner, J., & Yeager, S. (2020). The value of initialization on decadal timescales: State-dependent predictability in the CESM decadal prediction large ensemble. *Journal of Climate*, 33(17), 7353–7370. <https://doi.org/10.1175/JCLI-D-19-0571.1>
- Clement, A., Bellomo, K., Murphy, L. N., Cane, M. A., Mauritsen, T., R  del, G., & Stevens, B. (2015). The Atlantic Multidecadal Oscillation without a role for ocean circulation. *Science*, 350(6258), 320–324. <https://doi.org/10.1126/science.aab3980>
- Danabasoglu, G. (2019). *NCAR CESM2 model output prepared for CMIP6 CMIP historical*. Earth System Grid Federation. <https://doi.org/10.22033/ESGF/CMIP6.7627>
- Danabasoglu, G., Lamarque, J.-F., Bacmeister, J., Bailey, D. A., DuVivier, A. K., Edwards, J., et al. (2020). The community earth system model version 2 (CESM2). *Journal of Advances in Modeling Earth Systems*, 12(2), e2019MS001916. <https://doi.org/10.1029/2019MS001916>
- Enfield, D. B., Mestas-Nu  ez, A. M., & Trimble, P. J. (2001). The Atlantic multidecadal Oscillation and its relation to rainfall and river flows in the continental. *US Geophysical Research Letters*, 28(10), 2077–2080. <https://doi.org/10.1029/2000GL012745>
- Eyring, V., Bony, S., Meehl, G. A., Senior, C. A., Stevens, B., Stouffer, R. J., & Taylor, K. E. (2016). Overview of the Coupled Model Inter-comparison Project Phase 6 (CMIP6) experimental design and organization. *Geoscientific Model Development*, 9(5), 1937–1958. <https://doi.org/10.5194/gmd-9-1937-2016>
- Fang, S.-W., Khodri, M., Timmreck, C., Zanchettin, D., & Jungclauss, J. (2021). Disentangling internal and external contributions to Atlantic multidecadal variability over the past millennium. *Geophysical Research Letters*, 48(23). <https://doi.org/10.1029/2021gl095990>
- Fenske, T., & Clement, A. (2022). No internal connections detected between low frequency climate modes in North Atlantic and North Pacific basins. *Geophysical Research Letters*. <https://doi.org/10.1029/2022gl097957>
- Foster, D., Gagne, D. J., & Whitt, D. B. (2021). Probabilistic machine learning estimation of ocean mixed layer depth from dense satellite and sparse in situ observations. *Journal of Advances in Modeling Earth Systems*, 13(12). <https://doi.org/10.1029/2021ms002474>
- Frankignoul, C., & Hasselmann, K. (1977). Stochastic climate models, Part II Application to sea-surface temperature anomalies and thermocline variability. *Tellus*, 29(4), 289–305. <https://doi.org/10.1111/j.2153-3490.1977.tb00740.x>
- Giorgetta, M. A., Jungclauss, J., Reick, C. H., Legutke, S., Bader, J., B  ttinger, M., et al. (2013). Climate and carbon cycle changes from 1850 to 2100 in MPI-ESM simulations for the Coupled Model Intercomparison Project Phase 5. *Journal of Advances in Modeling Earth Systems*, 5(3), 572–597. <https://doi.org/10.1002/jame.20038>
- Gordon, E. M. (2022). emily-gordy/Decadal-SST-prediction: Decadal SST prediction, revised GRL submission. <https://doi.org/10.5281/zenodo.6646950>
- Gordon, E. M., Barnes, E. A., & Hurrell, J. W. (2021). Oceanic harbingers of Pacific decadal oscillation predictability in CESM2 detected by neural networks. *Geophysical Research Letters*, 48(21). <https://doi.org/10.1029/2021gl095392>
- Guillaumin, A. P., & Zanna, L. (2021). Stochastic-deep learning parameterization of ocean momentum forcing. *Journal of Advances in Modeling Earth Systems*, 13(9). <https://doi.org/10.1029/2021ms002534>
- Henley, B. J., Gergis, J., Karoly, D. J., Power, S., Kennedy, J., & Folland, C. K. (2015). A tripole index for the interdecadal Pacific oscillation. *Climate Dynamics*, 45(11), 3077–3090. <https://doi.org/10.1007/s00382-015-2525-1>
- Hurrell, J. W., Holland, M. M., Gent, P. R., Ghan, S., Kay, J. E., Kushner, P. J., et al. (2013). The community earth system model: A framework for collaborative research. *Bulletin of the American Meteorological Society*, 94(9), 1339–1360. <https://doi.org/10.1175/BAMS-D-12-00121.1>
- Labe, Z. M., & Barnes, E. A. (2022). Predicting slowdowns in decadal climate warming trends with explainable neural networks. <https://doi.org/10.1002/essoar.10508874.2>
- Mann, M. E., Steinman, B. A., Brouillette, D. J., & Miller, S. K. (2021). Multidecadal climate oscillations during the past millennium driven by volcanic forcing. *Science*, 371(6533), 1014–1019. <https://doi.org/10.1126/science.abc5810>
- Mantua, N. J., Hare, S. R., Zhang, Y., Wallace, J. M., & Francis, R. C. (1997). A Pacific interdecadal climate oscillation with impacts on salmon production. *Bulletin of the American Meteorological Society*, 78(6), 1069–1080. [https://doi.org/10.1175/1520-0477\(1997\)078<1069:APICOW>2.0.CO;2](https://doi.org/10.1175/1520-0477(1997)078<1069:APICOW>2.0.CO;2)
- Mariotti, A., Baggett, C., Barnes, E. A., Becker, E., Butler, A., Collins, D. C., et al. (2020). Windows of opportunity for skillful forecasts subseasonal to seasonal and beyond. *Bulletin of the American Meteorological Society*, 101(5), E608–E625. <https://doi.org/10.1175/BAMS-D-18-0326.1>
- Mayer, K. J., & Barnes, E. A. (2021). Subseasonal forecasts of opportunity identified by an explainable neural network. *Geophysical Research Letters*, 48(10), e2020GL092092. <https://doi.org/10.1029/2020GL092092>
- Meehl, G. A., Hu, A., Arblaster, J. M., Fasullo, J., & Trenberth, K. E. (2013). Externally forced and internally generated decadal climate variability associated with the interdecadal Pacific oscillation. *Journal of Climate*, 26(18), 7298–7310. <https://doi.org/10.1175/JCLI-D-12-00548.1>
- Meehl, G. A., Hu, A., & Teng, H. (2016). Initialized decadal prediction for transition to positive phase of the Interdecadal Pacific Oscillation. *Nature Communications*, 7(1), 11718. <https://doi.org/10.1038/ncomms11718>
- Meehl, G. A., Richter, J. H., Teng, H., Capotondi, A., Cobb, K., Doblas-Reyes, F., et al. (2021). Initialized Earth System prediction from subseasonal to decadal timescales. *Nature Reviews Earth & Environment*, 2(5), 340–357. <https://doi.org/10.1038/s43017-021-00155-x>
- Merryfield, W. J., Baehr, J., Batt  , L., Becker, E. J., Butler, A. H., Coelho, C. A. S., et al. (2020). Current and emerging developments in subseasonal to decadal prediction. *Bulletin of the American Meteorological Society*, 101(6), E869–E896. <https://doi.org/10.1175/BAMS-D-19-0037.1>
- Msadek, R., Dixon, K. W., Delworth, T. L., & Hurlin, W. (2010). Assessing the predictability of the Atlantic meridional overturning circulation and associated fingerprints. *Geophysical Research Letters*, 37(19). <https://doi.org/10.1029/2010gl044517>
- Okumura, Y. M., & Deser, C. (2010). Asymmetry in the duration of El Ni  o and La Ni  a. *Journal of Climate*, 23(21), 5826–5843. <https://doi.org/10.1175/2010JCLI3592.1>
- Pohlmann, H., Botzet, M., Latif, M., Roesch, A., Wild, M., & Tschuck, P. (2004). Estimating the decadal predictability of a coupled AOGCM. *Journal of Climate*, 17(22), 4463–4472. <https://doi.org/10.1175/3209.1>
- Power, S., Casey, T., Folland, C., Colman, A., & Mehta, V. (1999). Inter-decadal modulation of the impact of ENSO on Australia. *Climate Dynamics*, 15(5), 319–324. <https://doi.org/10.1007/s003820050284>
- Schulzweida, U. (2019). CDO user guide. <https://doi.org/10.5281/zenodo.3539275>
- Simpson, I. R., Deser, C., McKinnon, K. A., & Barnes, E. A. (2018). Modeled and observed multidecadal variability in the North Atlantic jet stream and its connection to sea surface temperatures. *Journal of Climate*, 31(20), 8313–8338. <https://doi.org/10.1175/JCLI-D-18-0168.1>
- Simpson, I. R., Yeager, S. G., McKinnon, K. A., & Deser, C. (2019). Decadal predictability of late winter precipitation in western Europe through an ocean–jet stream connection. *Nature Geoscience*, 12(8), 613–619. <https://doi.org/10.1038/s41561-019-0391-x>
- Toms, B. A., Barnes, E. A., & Ebert-Uphoff, I. (2020). Physically interpretable neural networks for the geosciences: Applications to Earth system variability. *Journal of Advances in Modeling Earth Systems*, 12(9), e2019MS002002. <https://doi.org/10.1029/2019MS002002>
- Toms, B. A., Barnes, E. A., & Hurrell, J. W. (2021). Assessing decadal predictability in an earth–system model using explainable neural networks. *Geophysical Research Letters*, 48(12). <https://doi.org/10.1029/2021gl093842>
- Trenberth, K. E., & Fasullo, J. T. (2013). An apparent hiatus in global warming? *Earth's Future*, 1(1), 19–32. <https://doi.org/10.1002/2013ef000165>

- Trenberth, K. E., & Shea, D. J. (2006). Atlantic hurricanes and natural variability in 2005. *Geophysical Research Letters*, 33(12), L12704. <https://doi.org/10.1029/2006gl026894>
- van der Velden, E. (2020). CMasher: Scientific colormaps for making accessible, informative and 'cmashing' plots. *The Journal of Open Source Software*, 5(46), 2004. <https://doi.org/10.21105/joss.02004>
- Wu, S., Liu, Z., Zhang, R., & Delworth, T. L. (2011). On the observed relationship between the Pacific decadal oscillation and the Atlantic multi-decadal oscillation. *Journal of Oceanography*, 67(1), 27–35. <https://doi.org/10.1007/s10872-011-0003-x>
- Xie, S.-P., & Tanimoto, Y. (1998). A pan-Atlantic decadal climate oscillation. *Geophysical Research Letters*, 25(12), 2185–2188. <https://doi.org/10.1029/98GL01525>
- Yeager, S. G., Danabasoglu, G., Rosenbloom, N. A., Strand, W., Bates, S. C., Meehl, G. A., et al. (2018). Predicting near-term changes in the Earth system: A large ensemble of initialized decadal prediction simulations using the community Earth system model. *Bulletin of the American Meteorological Society*, 99(9), 1867–1886. <https://doi.org/10.1175/BAMS-D-17-0098.1>
- Zhang, R., & Delworth, T. L. (2006). Impact of Atlantic multidecadal oscillations on India/Sahel rainfall and Atlantic hurricanes. *Geophysical Research Letters*, 33(17), L17712. <https://doi.org/10.1029/2006gl026267>
- Zhang, R., Sutton, R., Danabasoglu, G., Kwon, Y.-O., Marsh, R., Yeager, S. G., et al. (2019). A review of the role of the Atlantic meridional overturning circulation in Atlantic multidecadal variability and associated climate impacts. *Review of Geophysics*, 57(2), 316–375. <https://doi.org/10.1029/2019rg000644>
- Zhang, Y., Wallace, J. M., & Battisti, D. S. (1997). ENSO-Like interdecadal variability: 1900–93. *Journal of Climate*, 10(5), 1004–1020. [https://doi.org/10.1175/1520-0442\(1997\)010<1004:ELIV>2.0.CO;2](https://doi.org/10.1175/1520-0442(1997)010<1004:ELIV>2.0.CO;2)

References From the Supporting Information

- Mamalakis, A., Barnes, E. A., & Ebert-Uphoff, I. (2022). Investigating the fidelity of explainable artificial intelligence methods for applications of convolutional neural networks in geoscience. *ArXiv*. Retrieved from <http://arxiv.org/abs/2202.03407>
- Mamalakis, A., Ebert-Uphoff, I., & Barnes, E. A. (2021). Neural network attribution methods for problems in geoscience: A novel synthetic benchmark dataset. *ArXiv*. Retrieved from <http://arxiv.org/abs/2103.10005>